Astron. Astrophys. 356, 1031–1038 (2000)

ASTRONOMY
AND
ASTROPHYSICS

Structure, star formation and magnetic fields in the OMC1 region

K.E.K. Coppin, J.S. Greaves⋆, T. Jenness⋆⋆, and W.S. Holland⋆⋆⋆

Joint Astronomy Centre, 660 N. A'ohōkū Place, University Park, Hilo, HI 96720, USA

Received 1 September 1999 / Accepted 25 November 1999

Abstract. We present the results of a study of the submillimetre wavelength continuum emission, at 450 and 850 μm, encompassing the OMC1 region in the northern part of the Orion A cloud, and focusing on the structure and star formation in an area of about $\sim$70 arcmin^2 ($\sim$1.2 pc^2). Our observations are 3 times deeper in flux than previous submillimetre observations of this region and we have found a number of pre-stellar dust clumps in the region from which mass functions were determined. Our clump mass functions include objects down to 0.1 $M_\odot$ and the power-law slope of –1.5 is similar to that generally found from spectral line observations of molecular gas clumps. The data do not show the steeper slope of –2.5 for masses above 0.5 $M_\odot$ identified by Motte et al. (1998) in dust maps of the ρ Ophiuchus low-mass star-forming region, possibly indicating different collapse processes. Polarimetry data for the north-east bar and KL regions of OMC1 were also obtained, and it is apparent that the field orientations with respect to cloud elongation differ between star-forming and non-star-forming regions. The main OMC1 ridge is consistent with collapse down field lines while the north-east bar has a field structure roughly outlining the HII region. The dominant physical processes apear to be pressure from the expanding HII region and fragmentation on the Jeans scale, rather than magnetic effects.

Key words: polarization – stars: formation – ISM: individual objects: OMC1 – ISM: magnetic fields – ISM: structure

1. Introduction

The Orion Molecular Cloud (OMC) is the closest region of high-mass star-formation to the Sun, at $\sim$ 450 pc, and has consequently been much studied. The most prominent region in maps of the molecular gas is the OMC1 cloud, which contains several luminous star-forming cores (Chini et al. 1997) and energetic outflows (Schmid-Burgk et al. 1989) plus a large number of young stars visible in the infra-red (e.g. McCaughrean & Stauffer 1994). The main ridge of gas and dust lies to the west of the HII region around the bright Trapezium stars (e.g. Johnstone & Bally 1999), and to the south-east lies the 'Bright Bar' which is an ionization/shock front seen roughly edge-on (e.g. Hogerheijde et al. 1995, and references therein).

In this paper, we address the question of the sub-structure of the gas and dust in OMC1, and how this relates to the initial mass function (IMF) of the stars that are forming. One of the least biased methods of identifying cores or clumps is mapping of the dust emission in the submillimetre regime, since this is largely optically thin, and the fluxes depend only on the grain temperature and emissivity. In contrast, observations of trace molecules in the H_2 gas are subject to strong local variations such as density-dependent excitation and chemical abundances.

Imaging projects for star-forming clouds are thus taking advantage of the first generation of submillimetre cameras; for example, Motte et al. (1998) have recently mapped a 1 pc^2 area in the ρ Ophiuchus low-mass star-forming cloud with an unprecedented sensitivity down to 0.1 $M_\odot$ cores. The aim of the present paper is to make a study of similar area and sensitivity in the OMC1 cloud for high-mass star-forming cores; this work is complementary to the wide-field mapping of OMC1 by Johnstone & Bally (1999) but about 3 times deeper in flux. We also present some early results from submillimetre imaging polarimetry, to compare the magnetic field structures in evolved and quiescent cores in OMC1.

2. Observations

The Orion Molecular Cloud data was observed with 7.″5 resolution at 450 μm and 14″ resolution at 850 μm with the 15 m James Clerk Maxwell Telescope (JCMT) atop of Mauna Kea in Hawaii in December of 1997. "Jiggle map" data were obtained simultaneously at both wavelengths with SCUBA (Submillimetre Common-User Bolometer Array) which is comprised of two hexagonal arrays of 91 bolometers at 450 μm and 37 bolometers at 850 μm, and has a field of view of about 2.′3. Some "scan map" images were also obtained at these wavelengths to complete the final images. Refer to Holland et al. (1999) for further information on SCUBA and mapping modes. Polarimetry data were taken in January 1999 with a rotating half-wave plate and a fixed etched grid in front of the SCUBA window, so that the bolometers see one plane of polarization, but the

Send offprint requests to: J.S. Greaves
⋆ j.greaves@jach.hawaii.edu
⋆⋆ t.jenness@jach.hawaii.edu
⋆⋆⋆ w.holland@jach.hawaii.edu

Table 1. Large cloud features $> 1'$ in the 850 μm map (Fig. 1), listing centre positions relative to the bright IRc2 source (0,0) at RA(1950)=$05^h32^m47.0^s$, Dec(1950)=$-05^\circ24'26''$. Total fluxes in Jy (summed from a Jy/pixel scale based on extended-flux calibration) are given at 850 μm and 450 μm. It should be noted that the KL and S overlap region contains about 107 Jy of flux at 850 μm and 1,481 Jy of flux at 450 μm.

		850 μm	450 μm	
δRA ($''$)	δDec ($''$)	$S_{\rm tot}$ (Jy)		Location
8	-224	59	—	Bright Bar-South
-5	-85	262	3924	Orion S
2	6	657	7304	Orion KL
45	198	113	1796	North

source polarization plane is effectively rotated to modulate the signal. Jiggle maps were obtained at waveplate positions 22.5° apart and the polarized signal was analysed with the POLPACK software package, as described by Greaves et al. (2000).

The SURF (SCUBA User Reduction Facility; Jenness & Lightfoot 1998) and KAPPA (Currie & Berry 1999) reduction packages were used for flat-fielding, extinction correction, sky noise removal, despiking, removal of bad pixels, rebinning and calibration of the images. A variety of calibration sources including Uranus, Mars, OH231.8 and CRL618 were used from the nights of the observations and also from nights surrounding the observing nights to check how much the gain (Jy/V conversion factor) varied. There was only a small gain gradient during the night at 850 μm so an average value of 270 Jy/beam per volt was taken. For 450 μm, however, there was a steep slope in the gain values (ranging from 465–1400 Jy/beam per volt) so a plot of gain versus time was used to interpolate appropriate gain values at the time the observations were made. Calibration uncertainties are $\approx$ 10% at 850 μm and $\approx$ 20% at 450 μm and are due mainly to fluctuations in the atmospheric transmission and temperature-induced changes in the dish surface accuracy.

Nine overlapping fields of view were observed over two nights, with zenith opacities obtained from skydips at 850 (450) μm ranging from 0.17(0.91) to 0.66(3.82). The 'Bright Bar' region was observed only on the second night when the conditions were poor for 450 μm work, so this area has not been included in the final 450 μm jiggle mosaic. The individual reduced images were checked for internal consistency of maximum and minimum values, and also of integrated flux per field. Each image was also compared to its neighbouring frame(s) to check that the flux levels were even across any overlap region(s). Each jiggle map was then identified on the scan map and checked to see if any of the chop throws were onto bright regions. Areas in the jiggle map where the flux differed by more than 30% from the scan map were removed (changing this threshold in the range 20–40% did not significantly affect the size of the trimmed area).

Direct measurements of the noise levels in the maps were not possible as there are very few blank regions. Thus noise equivalent flux densities (NEFD's) were estimated from the sky transmission and known bolometer performance, yielding final 3σ noise levels of 0.045 Jy/beam $\pm$ 20% at 850 μm and 0.3 Jy/beam $\pm$ 6% at 450 μm respectively (variations are from transmission differences), for 0.7 hours of integration per field. Any clumps detected above these levels therefore have a 99% chance of being real if the noise has Gaussian statistics. The scan map data, which cover a 10 $\times$ 10 arcmin area[1], have 1σ noise levels estimated from the NEFD's of the order of $\sim$0.1 Jy/beam at 850μm and $\sim$1.5 Jy/beam at 450 μm; they are included in the final images produced by mosaicing the jiggle and scan data (Fig. 1) but the high-noise areas are not used in the data analysis. The scan data were given a lower weight in the rebinning process and used simply to fill in gaps in the jiggle mosaic.

The peak flux of the OMC1 region lies in the bright clump centred on IRc2, often referred to as Orion BN/KL, and is 136 Jy/beam at 850 μm and 402 Jy/beam at 450 μm. We compared these values to other published JCMT results of 167 Jy/beam at 850 μm and 490 Jy/beam at 450 μm. We obtained $\sim$80% of the flux that Johnstone & Bally (1999) obtained from scan-map data, in good agreement given the difficulties of absolute calibration and possible chopping onto low-level emission in the jiggle-map data.

3. Data analysis and results

3.1. General structure

The general structure of the OMC1 dust emission (Fig. 1) includes the main north-south ridge, the Bright Bar to the south-east and another weaker bar to the north-east, more readily apparant in molecular gas emission (Greaves & Church 1996). Several large structures have been identified using the SExtractor (Bertin & Arnouts 1996) package within the GAIA display tool (two of these structures overlap due to the constraint of an elliptical shape). These features are contiguous 'clouds' with major axes $>$ 1 arcmin (0.13 pc for a source distance of 450 pc), and their fluxes in Jy are listed in Table 1. Together they contain about 65–90% of the total flux in the molecular clouds around the central HII region.

There is a good general correspondence to the structure seen in molecular line images, such as the ^{13}CO J=2–1 (1.35 mm) maps obtained by Greaves & Church (1996) and White & Sandell (1995). We have identified 8 major peaks with offset differences between the line and continuum datasets being no more than $\sim$20$''$. Two other ^{13}CO peaks do not seem to be identifiable with clumps in the continuum maps. The details of the clump appearance differ somewhat between the line and continuum datasets as expected from the discussion above, but both seem to show roughly the same cores.

A key use of spectral line data is to estimate the 'contamination' within the SCUBA filter passbands. We adopt for spectral line contribution a value of 60% for Orion-KL at 850 μm and 10% for more typical clumpy regions based on observations of the Orion-KL and S region made by Groesbeck (1995). We neglect the 10% contributions in the following tables of flux levels,

[1] Fig. 1 displays only an area of $\sim$ 7 $\times$ 10 arcmin.

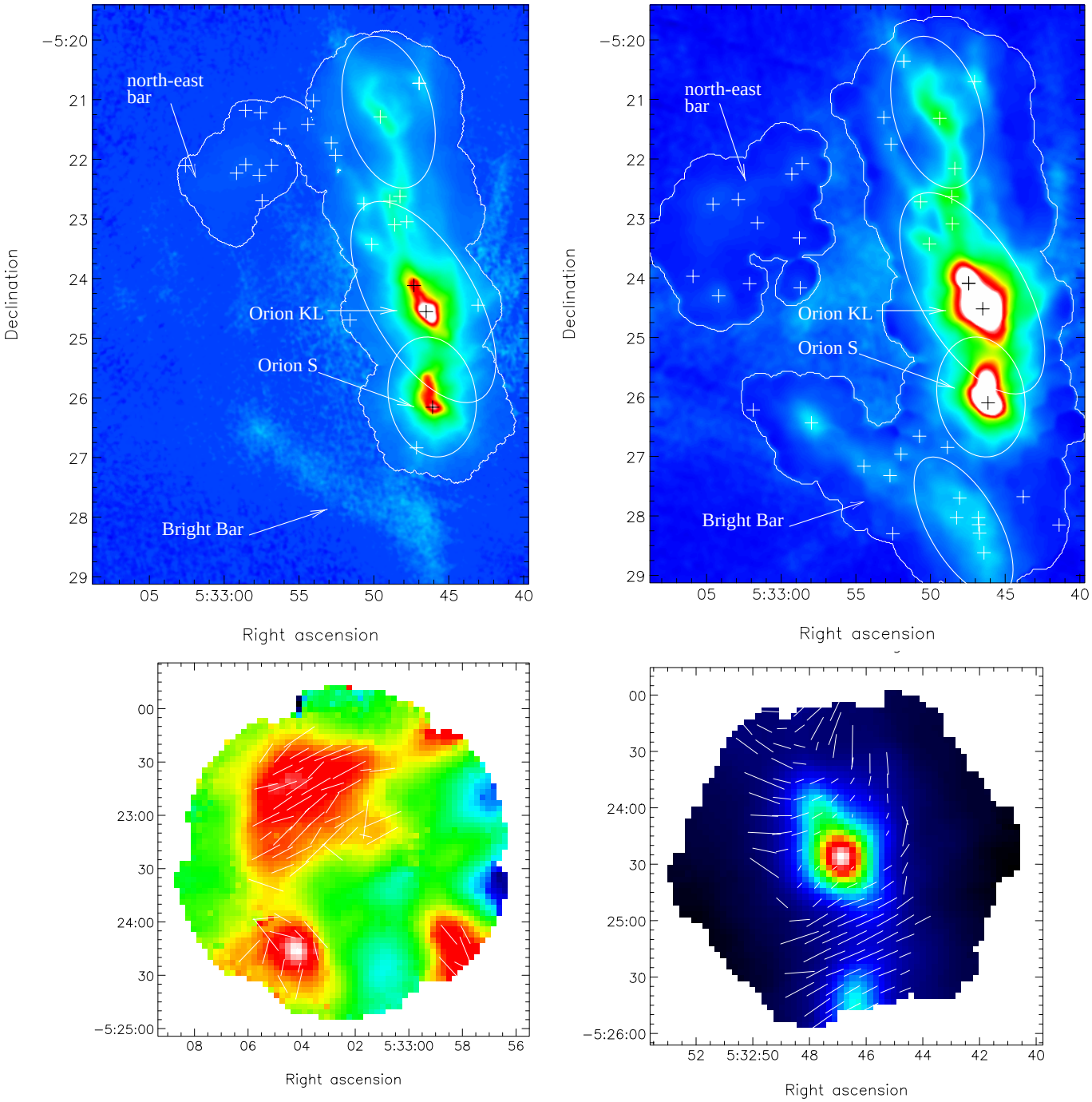

Fig. 1. Combined jiggle and scan map images, with an outline of the jiggle map area used at 450 μm (top left) and at 850 μm (top right). Clumps are marked by the '+' signs and the ellipses drawn represent the large cloud features found by the SEXTRACTOR package. The images are each approximately $7' \times 10'$, equivalent to 1.2 parcsec^2. The lower images show the KL and north-east bar regions (upper left and centre right in the flux maps), overlaid with the 850 μm polarization vectors — these are rotated 90° to show the deduced magnetic field directions. The largest vector in each plot is 15%. All polarimetric detections are better than 3σ (3σ defines the position angle to $\pm$ 10%).

as it is a small fraction that is expected to be relatively constant for quiescent clumps. At 450 μm, the broad-band spectral survey of Serabyn & Weisstein (1995) suggests a line flux about 3.5 times higher than at 850 μm, but the dust flux will be 11 times higher for a dust opacity index of ~ 1.8 (Lis et al. 1998), so the contamination is likely to be only about 30% at 450 μm.

3.2. Clump identification

In order to identify features on smaller scales, the centroiding task in KAPPA (Currie & Berry 1999) was used to detect peaks above the 3σ level in beamsize areas. Sources were rejected using several test criteria:

1. part of a clump being truncated by the map edge,
2. having a negative flux (due to the problem of chopping onto a brighter region),
3. having a higher mean signal in larger areas (i.e. a bowl not a peak), and
4. having a peak flux above the local background lower than the noise cut-off.

Clumps in adjacent beams were accepted if they were further than 5″ apart and appeared as visually distinct in the maps. The majority of rejected clumps arose from (1) above; for example, in the 850 μm jiggle mosaic there were nine edge features and one each of a bowl and a negative flux.

For the remaining clumps, the fluxes of the peaks above the local background were calculated using the relation

$$S_{\rm clump} = \frac{4}{3}(\overline{S}_{\rm beam} - \overline{S}_{\rm 2beam}), \quad (1)$$

where $\overline{S}_{\rm beam}$ is the average flux in a beamsize circle about the centroid and $\overline{S}_{\rm 2beam}$ is the average flux in a circle twice the beamsize. This procedure is very simple to run, and has few free parameters. More sophisticated fitting algorithms were found not to perform well in the highly complex structure of OMC1, as the larger 'clouds' (Table 1) tend to be identified instead of the clumps. The wavelet analysis used for ρ Ophiuchus by Motte et al. (1998) to identify 15–30″ diameter clumps works somewhat differently from our centroiding algorithm, but the procedures for subtracting background emission are similar.

In total, 39 clumps at 850 μm and 28 clumps at 450 μm were detected above the noise levels and verified (Table 2), for 55 sources in the final catalogue. Clump positions are listed relative to the (0,0) position for IRc2, at RA(1950)=$05^h32^m47.0^s$, Dec(1950)=$-05^\circ 24' 26''$.

Hypothetically, up to ∼4 times as many clumps could be identified at 450 μm as the beam sized areas are about four times smaller than at 850 μm. At the other extreme, if the clumps are widely spaced they would all be seen in both maps, giving the same total number. In fact, given that ∼90% of the full jiggle map area was used at 850 μm but only ∼45% at 450 μm (due to the lack of good Bright Bar data and a slightly smaller jiggle-map field of view), we would expect to see between 0.5 and 2 times as many clumps at the shorter wavelength. The actual ratio is 0.72, confirming that the clumps are quite well spaced.

Clumps identified at 850 μm are present in the 450 μm map also (Table 2), ruling out the possibility of false identifications. There are only 3 clumps in the areas common to both maps that are *not* seen also at 450 μm, and all have some emission at 450 μm although not a distinct centroid. It was expected that there might be some confusion due to binary clumps in the 450 μm map which appear as elongated single clumps in the 850 μm map, purely by a resolution effect. We found that the clumps are generally circular in shape (with respect to the FWHM profiles), however, at 850 μm 7 of the clumps are elongated (axis ratios ≥ 2:1), and at 450 μm 4 are elongated. Only two of these clumps at 850 μm are identified as binaries in the 450 μm map, while the rest of the elongated clumps at 850 μm are in areas excluded from the 450 μm map area.

Table 2. Fluxes above the background $S_{\rm c}$, enhancement relative to the background $S_{\rm c}/S_{\rm b}$, and 2+β values for OMC1 clumps. For Orion-KL, values listed are 40% (70%) of the observed flux at 850 (450) μm due to line contamination.

		850 μm		450 μm		
δRA ($''$)	δDec ($''$)	$S_{\rm c}$ (Jy/beam)	$S_{\rm c}/S_{\rm b}$	$S_{\rm c}$ (Jy/beam)	$S_{\rm c}/S_{\rm b}$	2 + β
−2	−246	0.35	0.10			
89	−227	0.07	0.09			
3	−226	0.25	0.07			
4	−218	0.21	0.06			
−77	−218	0.07	0.25			
26	−211	0.16	0.05			
4	−211	0.27	0.07			
23	−191	0.29	0.08			
−41	−190	0.06	0.09			
92	−168	0.41	0.16			
119	−159	0.41	0.17			
81	−147	0.36	0.17			
35	−140	0.07	0.03			
9	−139			2.20	0.11	
63	−129	0.10	0.06			
171	−115	1.02	0.27			
229	−102	0.07	0.26			
−6	−95	14.43	0.35	53.55	0.25	2.38
76	−11			1.07	0.11	
0	0	19.36	0.45	68.49	0.27	—
−52	4			1.68	0.06	
264	13	0.48	0.35			
182	21	0.41	0.46			
233	25	0.08	0.32			
14	26	13.60	0.31	45.26	0.24	1.64
289	33	0.05	0.10			
53	65	1.13	0.19	3.80	0.11	2.87
183	71	0.12	0.26			
30	85	1.23	0.17	5.49	0.12	2.65
225	87	0.09	0.14			
19	88			3.39	0.09	
269	105	0.17	0.15			
62	108	1.41	0.29	4.81	0.15	2.50
163	109			0.35	0.25	
36	109			4.79	0.10	
244	110	0.07	0.08			
30	113	1.70	0.20	4.63	0.09	2.16
166	135			0.85	0.19	
191	137	0.24	0.25	0.32	0.07	1.91
28	141	1.29	0.23			
240	145			0.76	0.34	
154	145			0.31	0.12	
180	146	0.21	0.19	0.71	0.14	2.51
90	155			1.11	0.11	
91	166	0.45	0.20	1.51	0.13	2.97
146	182			0.71	0.34	
118	186			0.77	0.20	
43	192	1.87	0.24	8.82	0.18	2.81
98	193	0.25	0.13			
165	198			0.50	0.25	
180	200			0.31	0.27	
112	210			1.29	0.19	
−31	225			1.13	0.18	
8	229	0.89	0.22	4.76	0.18	2.98
78	250	0.49	0.16			

We conclude that the problem of merged clumps is negligible for statistical purposes. Also, most of the observed clump FWHM are comparable in size to the beams at both wavelengths, and so the cores must be close to point-like. A clump mass function based on flux per beam-sized circle will therefore be accurate apart from a few objects. At 850 μm there are 2 (out of 39 clumps) larger than the beam by ∼50%. At 450 μm there is 1 (out of 28 clumps) which is bigger than the beam by ∼50%. Finally, faint clumps may be missed by the centroiding task if they are near to a very bright feature, and this would also affect the mass function. By adding simulated clumps to the 850 μm mosaic, we estimate that secondary features offset by a few tens of arcseconds and less than ~ 5 % in relative brightness will go undetected. However, there are only a few bright clumps whose hypothetical neighbours would be above our flux cutoff in the mass function (see below).

Clumps turned out to be typically ∼20% of the flux within their beamsize region, at both 450 μm and at 850 μm. This is only weakly dependent on the brightness of the clumps (e.g. increases to 27% for the 10 brightest clumps at 850 μm, with fluxes above 1 Jy) and is very similar at the two wavelengths. The flux in identified clumps is $<$ 7% of the total flux of the whole jiggle-map region (14,251 Jy at 450 μm and 1,324 Jy for the larger region at 850 μm). The great majority of the material is thus in the ambient cloud, not condensed into clumps.

The spectral slopes between 450 and 850 μm were fitted assuming a modified blackbody in the Rayleigh-Jeans regime, $S_\nu \propto \nu^{2+\beta}$, and the $2+\beta$ values for the clumps are given in Table 2. The IRc2 position was omitted as the relative contributions of line and continuum flux for the clump and the local background are not accurately known. The mean β-index for the 11 remaining clumps detected at both wavelengths is 0.5. This is distinctly lower than the values of 1.75 to 2.5 found by Lis et al. (1998) from 350 and 1100μm maps smoothed to 31″ resolution. Our 450 and 850 μm fluxes for the large 'clouds' listed in Table 1 also give high β values, of around 1.8 to 2.3, although with an error of about $\pm$ 0.5 from the calibration uncertainties. We conclude that grain growth has probably occurred in the dense cores, producing larger particles that behave more like blackbodies at long wavelengths, whereas the extended cloud material has smaller grains that do not emit efficiently in the submillimetre regime.

3.3. Clump mass function

Mass functions were determined at both wavelengths, by assuming that the number of clumps dN in a mass bin M to $M+dM$ is given by $\frac{dN}{dM} \propto M^{-\alpha}$. It was also assumed that the clump flux, $S_{\rm clump}$, directly traces the mass M, if β and $T_{\rm dust}$ are approximately constant and the emission is optically thin throughout the entire region. The range of β values is quite limited (Table 2) and apart from the KL core, gas temperatures have been estimated at 25–30 K across our map (Greaves 1996). For simplicity we have treated the KL clump as having this same temperature, but note that if $T_{\rm dust}$ were $\sim$ 70 K, it would move down one bin in each plot. The only correction made was subtracting 60% of the observed flux for Orion KL at 850 μm and 30% at 450 μm due to line contamination as discussed earlier in the paper.

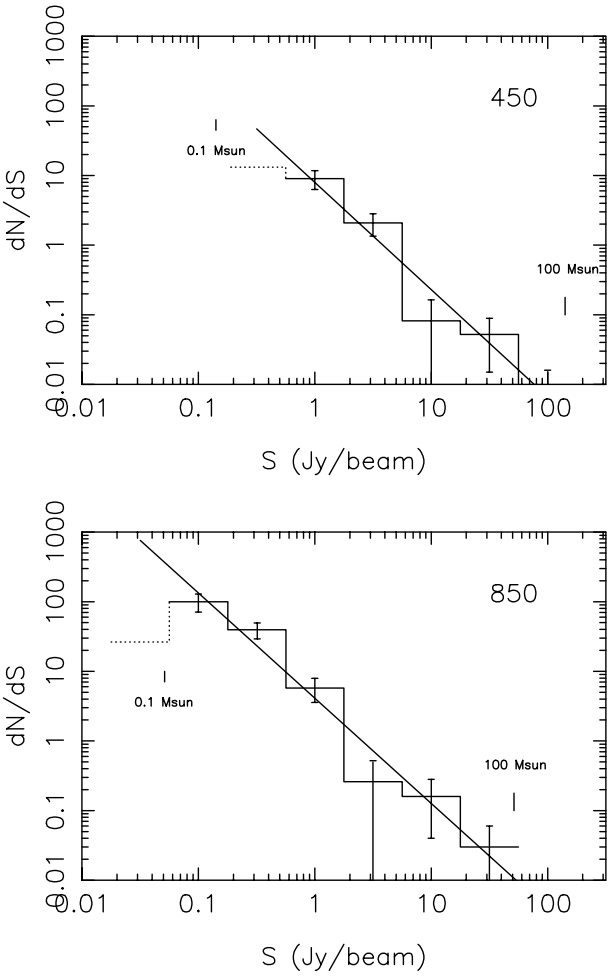

Fig. 2. Histograms of $\log dN/dS_{\rm clump}$ versus $\log S_{\rm clump}$ for clumps found at 450 μm and 850 μm.

The flux values were divided into logarithmic bins of width 0.5, and a histogram of $\log \frac{dN}{dS_{\rm clump}}$ versus $\log S_{\rm clump}$ was plotted (Fig. 2). The mass (flux) function equation was then fitted to it using simple linear regression; we ignored the lowest flux bin in each plot which is underfilled, as the lower bound is only at the 1–2σ level. Values of 1.51 (r=-0.98) and 1.54 (r=-0.98) were obtained for α at 850 μm and 450 μm respectively, where r is the correlation coefficient (r=-1 being a perfect fit). The probabilities of obtaining these results by chance from randomly distributed data are only about 0.1–0.5%. The fit quality to a single power law distribution is thus excellent, even though the clump masses range from about 0.1 to 100 $M_\odot$ (Fig. 2).

The mass function will be incomplete if faint clumps near bright peaks have been missed, and this could introduce a bias in the sense of an artificially flat slope at low flux values. For OMC1, this effect is unlikely to be large, based on number counts for the 850 μm mosaic. There are 10 clumps brighter than 1 Jy/beam, and if these have undetected neighbouring peaks

$\leq 5\%$ in brightness (see above), they are missing from the lowest three mass bins of Fig. 2. In a worst-case scenario, for example if all these clumps were surrounded by six adjacent peaks, α should be increased from 1.51 to 1.73.

Mass limits were calculated, assuming a dust temperature of 30 K (Greaves 1996) and adopting the dust mass emissivity values for protostellar cores used by Motte et al. (1998), corrected to 450 and 850 μm and taking a gas-to-dust mass ratio of 100. Assuming a value of 0.5 for β (Table 2), κ_{850} is 0.6 cm^{2}g^{-1} and κ_{450} is 0.85 cm^{2}g^{-1}, for the dust component alone. Masses calculated from these parameters approximately agree with previous calculations from spectral line observations; for example Greaves (1996) found 4–8 $M_\odot$ for the two brightest cores in the region 2 arcmin north of IRc2, and the dust data give about 4 $M_\odot$ in each case. Lis et al. (1998) adopted a dust emissivity and temperature of 2.5 cm^{2}g^{-1} and 55 K in the analysis of their 350 μm maps of OMC1, and this approach would give lower masses from our dust data. However, their map structures correlate with the hot gas traced by CO J=6–5 lines, while our maps resemble the cooler cores identified in ^{13}CO J=2–1, as discussed above.

3.4. Polarimetry data

Polarimetry results are shown in Fig. 1, for two contrasting regions — the Orion-KL core and the north-east bar. In the KL region, where young stars have formed, we deduce a largely linear field perpendicular to the dust ridge (with the standard assumption that the net field in the plane of the sky is orthogonal to the E-vector of the polarization). This is consistent with rapid collapse along the field lines, producing a flattened ridge, whereas collapse across the field has been inhibited by magnetic support. There is some evidence for 'hourglass' contraction of the field lines near KL, as discussed by Schleuning (1998). In contrast, the field directions for the less massive cores to the north-east are *along* the clump elongations, and appear to lie around the edges of the HII region (apart from a few vectors at the lower right). One possibility is that the rapid expansion of the HII region has created flattened clumps or filaments around its perimeter, and the magnetic field lines now form a 'shell' linking these structures. If these low-mass clumps are in a pre-collapse phase, we might expect the structure and field to be dominated by the large-scale energetics, rather than the limited dynamical evolution of the cores themselves.

The polarization percentages are broadly similar for both regions (Table 3), although there is a slight bias towards higher observed p% for the north-east bar — the 850 μm fluxes for the extended emission are only around 1 Jy/beam, implying that with our 2 hour integration, values of p less than $\sim 3.5\%$ would have detections less than 3-sigma. In general, polarization level is affected by grain alignment efficiency, inclination of the magnetic field to the plane of the sky and the degree of field structure unresolved by the telescope beam. The high polarizations seen in both parts of OMC1 suggest ordered fields with a low inclination to the sky and well-aligned grains. The low polarization seen towards IRc2 is consistent with field lines pulled in by the collapse process that formed the young stellar cluster, while no such polarization 'holes' have yet formed in the north-east cores.

Table 3. Summary of 850 μm polarization data in Fig. 1. For each region, the mean and standard deviation of the percentage polarization and inferred magnetic field direction are given by p and θ_B, for the number of vectors listed. The core regions are defined by flux levels above 25% of the peak, and the extended ridge positions are below the Orion-S 25% flux. The cores denoted A, B and C in the north-east bar are in anti-clockwise order from the top of the map (Fig. 1).

Location	N(vectors)	p (%)	θ_B (deg.)
Orion-KL	10	2.9 ± 1.2	124 ± 8
Orion-S	11	7.2 ± 1.5	117 ± 4
Ext. Ridge	77	7.3 ± 3.1	118 ± 37
NE-bar (A)	45	9.9 ± 2.9	121 ± 17
NE-bar (B)	6	5.5 ± 2.3	23 ± 32
NE-bar (C)	5	9.4 ± 1.3	39 ± 14

For the Orion-KL region, the polarizations are markedly higher than those seen in 450 and 350 μm data (Schleuning et al. 1997), observed with the HERTZ instrument on the Caltech Submillimeter Observatory 10.4m telescope. The spatial resolutions were similar (14″ and 18″ beams) and wavelength-independent results are expected for a single population of aligned grains with low optical depths. Comparing a set of 10 points with data at all three wavelengths within 9″ of the same position, we find that the position angles are in excellent agreement — mean differences are 1–4° between wavelengths, and the scatter on the differences is 5–10°, as expected from individual errors. However, the mean percentage polarization is 3% at 350 and 450 μm, but 7% at 850 μm, and there is a roughly constant increase at each point (for 850 versus 450 μm, a factor of 2.5 ± 1.25). There is unlikely to be an error in the 850 μm polarimetry, as Fig. 1 has 4 vectors in common with earlier 800 μm measurements by Aitken et al. (1997), and the percentages agree within factors of 0.8–1.3. There are also large polarizations of up to 8% in the 1300 μm data of Leach et al. (1991), although the comparison is less reliable as their beamsize of 30″ would have smoothed out some polarized structure.

Together these data suggest a single magnetic field direction but more than one population of grains along each line of sight, with varying polarizabilities and either different β-indices (Greaves et al. 1999) or different temperatures (Hildebrand et al. 1999). Future modelling of these results will be able to constrain the differences between the grain properties in the clumps and extended clouds.

4. Discussion

Motte et al. (1998) found the slope of the mass function α to be ~ 1.5 for clumps below ~ 0.5 $M_\odot$, but ~ 2.5 for clumps above 0.5 $M_\odot$, in their 1.3 mm study of star formation in the ρ Ophiuchus main cloud. Similarly, Testi & Sargent (1998) found a moderately steep slope of $\alpha = 2.1$ for clumps above ≈ 0.4 $M_\odot$ in a 3 mm dust emission survey of the Serpens molecular cloud.

These values are reminiscent of the stellar initial mass function, for example the Salpeter IMF with a slope of -2.35. However, when considering small-scale clumps and large-scale clumps together, Motte et al. (1998) found an overall $\alpha \sim 1.5$, which is typical of results based on spectral line observations of star-forming clouds (e.g. Blitz 1993). These results would suggest that clumps with stellar masses somehow decouple from the fragmentation process that forms clouds, producing a change to a steeper slope. Then, if a simple one clump-one star process occurs, with a constant fraction of the initial clump mass accreting onto the star, the clump mass function will have the same slope as the final IMF of the stars. Theory was developed by Nakano et al. (1995) on one clump-one star formation in Orion A.

In contrast, our data show only a slope of -1.5, although our lower mass bound of 0.1 $M_\odot$ is the same as for the ρ Oph study. The clump densities must also be similar, as the diameters are up to 30″ in ρ Oph and almost all less than 11″ in our OMC1 450 μm mosaic, and both these values correspond to approximately 0.025 pc at the respective cloud distances of 160 and 450 pc. Even if we rebin the 850 μm data, eliminating masses below the Motte et al. (1998) cutoff of 0.5 $M_\odot$ (fluxes below 250 mJy/beam), the slope does not significantly change (α = 1.4, r = -1.00 for 3 bins plus one empty bin, between log S = –0.35 and +1.15). Eliminating cores with young stars from the Orion survey also has little effect on the mass function, increasing α slightly to ~ 1.7, as only a few of the clumps have stellar activity such as outflows (KL, Orion-S and a core 2 arcmin north of KL, Greaves 1996). We have argued above that incompleteness is not a significant problem, again only increasing α to about 1.7 in a worst-case scenario. Thus the Orion data show a constant slope of about –1.5 for all masses, whereas the Ophiuchus data have a slope of –2.5 for clumps above about 0.5 $M_\odot$.

The changes in mass function slope are potentially a difference between regions of high-mass and low-mass star-formation, in the sense that the lower mass stars in each case may form by a similar process but the growth of more massive clumps could be inhibited. However, there may be statistical problems as there are only a few high-mass objects identified in each cloud. It is noteworthy that the slope appears to be anti-correlated with the upper mass boundary, with α-values of approximately 2.5, 2.1 and 1.5 in the Ophiuchus, Serpens and Orion surveys, for which the highest mass bins are centred on 3, 20 and 60 solar masses, respectively.

There are no obvious reasons to predict high-mass or low-mass star formation in Orion and Ophiuchus. The mass of the cloud material contained in clumps is similar in both cases, being up to $\sim 7\%$ in Orion and up to 10% in most of the Ophiuchus cores (although 2 of the 8 regions there do have higher fractions in clumps). Both clouds show similar filamentary structure and signs of induced star-formation, with dust ridges compressed by expansion of gas around the Trapezium and Sco OB2 stellar clusters, respectively. In addition, the spacing of the clumps appears to follow the same process. It is somewhat periodic in Ophiuchus, with separations of $\sim$0.03 pc (Motte et al. 1998), or about a Jeans length. In Orion, we find *two* distinct spacings, by calculating the distance of each clump from its nearest neighbour. The majority of the 850 μm clumps (28/39 or approximately 70%) have a neighbour in the range $24'' \pm 8''$, and the remaining 30% of clumps have a neighbour at $54'' \pm 7''$. The Jeans length is ~ 0.055 pc, or 25″, based on the Motte et al. (1998) formula and an initial density of 8×10^4 H_2 molecules cm^{-3} (estimated from the average 850 μm flux over the entire jiggle-map region, which gives 2500 $M_\odot$ over a diameter of 370″). Thus it appears that a clump has generally formed at the most compressed point of a sound wave through the cloud, as described by the Jeans scale, with a few 'missed' clumps so that a few spacings of two Jeans lengths occur between clumps.

5. Conclusions

We have mapped 850 and 450 μm continuum emission of the OMC1 region using the JCMT and SCUBA. We present a summary of our results and conclusions as follows:

1. 4 clouds larger than 0.1 pc contain most of the mass and flux in the region, while the 55 clumps identified on ~ 0.02 pc scales have $< 7\%$ of the total flux;
2. magnetic fields may have influenced the formation of the brightest cores, Orion-KL and Orion-S, but overall the HII region expansion and fragmentation on the Jeans length appear to be more important dynamically;
3. a single power-law function of slope –1.5 provides a good fit to the clump masses over a very wide range, from 0.1 to 100 $M_\odot$;
4. there is no distinction between the mass function for massive and low-mass cores, as was found for the much less luminous star-formation region, ρ Ophiuchus, by Motte et al. (1998).

Acknowledgements. The JCMT is operated by the Joint Astronomy Centre, on behalf of the UK Particle Physics and Astronomy Research Council, the Netherlands Organization for Pure Research, and the National Research Council of Canada. We would like to thank Doug Johnstone of CITA for providing access to his Orion images for flux comparisons, David Berry of STARLINK for assistance with the use of POLPACK, and an anonymous referee for very helpful comments. We would also like to thank the Joint Astronomy Centre, who funded Kristen Coppin's participation in this research.

References

Aitken D.K., Smith C.H., Moore T.J.T., et al., 1997, MNRAS 286, 85
Bertin E., Arnouts S., 1996, A&AS 117, 393
Blitz L., 1993, In: Levy E.H., Lunine J.I. (eds.) Protostars and Planets III, University of Arizona Press, p. 125
Chini R., Reipurth B., Ward-Thompson D., et al., 1997, ApJ 474, L135
Currie M.J., Berry D.S., 1999, Starlink User Note 95.14, Starlink Project, CLRC
Greaves J.S., 1996, MNRAS 280, 1293
Greaves J.S., Church S.E., 1996, MNRAS 283, 1179
Greaves J.S., Holland W.S., Minchin N.R., Murray A.G., Stevens J.A., 1999, A&A 344, 668
Greaves J.S., Jenness T., Chrysostomou A.C., Holland W.S., Berry D.S., 2000, In: Imaging at Radio through Submillimeter Wavelengths. ASP Conf. Ser., in press

Groesbeck T.D., 1995, Ph.D. Thesis, California Institute of Technology
Hildebrand R.H., Dotson J.L, Dowell C.D., Schleuning D.A., Vaillancourt J.E., 1999, ApJ 516, 834
Hogerheijde M.E., Jansen D.J., van Dishoeck E.F., 1995, A&A 294, 792
Holland W.S., Robson E.I., Gear W.K., et al., 1999, MNRAS 303, 659
Jenness T., Lightfoot J.F., 1998, In: Albrecht R., Hook R.N., Bushouse H.A. (eds.) Astronomical Data Analysis Software and Systems VII, ASP Conference Series Vol. 145, p. 216
Johnstone D., Bally J., 1999, ApJ 510, L49
Leach R.W., Clemens D.P., Kane B.D., Barvainis R., 1991, ApJ 370, 257
Lis D.C., Serabyn E., Keene J., et al., 1998, ApJ 509, 299
McCaughrean M.J., Stauffer J.R., 1994, AJ 108, 1382
Motte F., André P., Neri R., 1998, A&A 336, 150
Nakano T., Hasegawa T., Norman C., 1995, ApJ 450, 183
Schleuning D.A., Dowell C.D., Hildebrand R.H., Platt S.R., 1997, PASP 109, 307
Schleuning D.A., 1998, ApJ 493, 811
Schmid-Burgk J., Densing R., Krügel E., et al., 1989, A&A 215, 150
Serabyn E., Weisstein E.W., 1995, ApJ 451, 238
Testi L., Sargent A.I., 1998, ApJ 508, L91
White G.J., Sandell G., 1995, A&A 299, 179